Gabapentin Disrupts Binding of Perlecan to the $\alpha_2\delta_1$ Voltage Sensitive Calcium Channel Subunit and Impairs Skeletal Mechanosensation

Perla C. Reyes Fernandez[1], Christian S. Wright[1], Adrianna N. Masterson[2], Xin Yi[1], Tristen V. Tellman[3], Andrei Bonteanu[3,4], Katie Rust[1], Megan L. Noonan[5], Kenneth E. White[5], Karl J. Lewis[6], Uma Sankar[7], Julia M. Hum[8], Gregory Bix[9], Danielle Wu[3,4], Alexander G. Robling[7], Rajesh Sardar[2], Mary C. Farach-Carson[3,4], William R. Thompson[1,7,8]*

[1]Department of Physical Therapy, School of Health and Human Sciences, Indiana University, Indianapolis, IN 46202
[2]Department of Chemistry and Chemical Biology, School of Science, Indiana University, Indianapolis, IN 46202
[3]Department of Diagnostic and Biomedical Sciences, School of Dentistry, The University of Texas Health Science Center at Houston, Houston, TX 77054
[4]Department of Bioengineering, George R. Brown School of Engineering, Rice University, Houston, TX 77005
[5]Department of Medical and Molecular Genetics, School of Medicine, Indiana University, Indianapolis, IN 46202
[6]Meinig School of Biomedical Engineering, Cornell University, Ithaca, NY 14853
[7]Department of Anatomy, Cell Biology, & Physiology School of Medicine, Indiana University, Indianapolis, IN 46202
[8]Division of Biomedical Science, College of Osteopathic Medicine, Marian University, Indianapolis, IN 46222
[9]Departments of Neurosurgery and Neurology, School of Medicine, Tulane University, New Orleans, LA 70112

***Corresponding Author:** William R. Thompson, DPT, PhD
Email: thompwil@iu.edu
Ph.: (205) 975-2788

Running Title: Gabapentin impairs binding of perlecan and $\alpha_2\delta_1$

Disclosures: KEW receives royalties for licensing FGF23 to Kyowa Hakko Kirin Co., Ltd; had previous funding from Akebia, and current funding from Calico Labs. KEW also owns equity interest in FGF Therapeutics. All other authors have nothing to disclose.

This PDF file includes:

Main Text
Figures 1 to 5
Tables 1 to 3

Abstract

Our understanding of how osteocytes, the principal mechanosensors within bone, sense and perceive force remains unclear. Previous work identified “tethering elements” (TEs) spanning the pericellular space of osteocytes and transmitting mechanical information into biochemical signals. While we identified the heparan sulfate proteoglycan perlecan (PLN) as a component of these TEs, PLN must attach to the cell surface to induce biochemical responses. As voltage-sensitive calcium channels (VSCCs) are critical for bone mechanotransduction, we hypothesized that PLN binds the extracellular $\alpha_2\delta_1$ subunit of VSCCs to couple the bone matrix to the osteocyte membrane. Here, we showed co-localization of PLN and $\alpha_2\delta_1$ along osteocyte dendritic processes. Additionally, we quantified the molecular interactions between $\alpha_2\delta_1$ and PLN domains and demonstrated for the first time that $\alpha_2\delta_1$ strongly associates with PLN via its domain III. Furthermore, $\alpha_2\delta_1$ is the binding site for the commonly used pain drug, gabapentin (GBP), which is associated with adverse skeletal effects when used chronically. We found that GBP disrupts PLN::$\alpha_2\delta_1$ binding *in vitro*, and GBP treatment *in vivo* results in impaired bone mechanosensation. Our work identified a novel mechanosensory complex within osteocytes composed of PLN and $\alpha_2\delta_1$, necessary for bone force transmission and sensitive to the drug GBP. This work provides insights into the mechanisms underlying mechanotransduction and will inform future studies to understand the mechanisms responsible for the negative effects of GBP on bone.

Keywords: Perlecan, Voltage Sensitive Calcium Channels, Gabapentin, Mechanosensation, Bone

Introduction

Osteocytes reside deep within the mineralized matrix of bone and have long dendrite-like processes that run through microscopic channels called canaliculi[1]. As osteocytes are uniquely positioned in the bone matrix to communicate with other bone cell types via paracrine signaling and through direct contact with the cellular processes, they are considered the primary mechanosensory skeletal cells[1,2]. Transmission of mechanical force from the bone matrix to the osteocyte cell membrane was initially thought to occur via direct sensing of whole-tissue strains on the osteocyte surface. However, strains applied to whole bone *in vivo* during normal locomotion are typically between 0.04-0.3% (ref. 3,4), an order of magnitude smaller than the strain necessary to elicit a biochemical response at the osteocyte plasma membrane (1-10%) (ref. 5-7). Thus, a mechanism other than direct force transmission from the bone matrix must account for the ability of osteocytes to perceive mechanical input.

The pericellular space between (PCS) the bone matrix and the osteocyte plasma membrane contains non-mineralized extracellular matrix molecules, including proteoglycans, which are collectively termed the pericellular matrix (PCM)[8,9]. To explain the mechanism by which tissue-level mechanical strains are transmitted into biochemical responses in osteocytes, the presence of matrix-based "tethering elements" (TEs) able to span the PCS and anchor the osteocyte processes to the mineralized matrix was proposed[10]. This theoretical model was followed by ultrastructural studies using electron microscopy that visually revealed the tethering elements within the PCS[11]. However, the molecular identity of these TEs remained unknown.

Using immunostaining and immunogold assays, we showed that the large heparan sulfate proteoglycan perlecan (HSPG2, PLN) is expressed along osteocyte cell bodies and dendritic processes in cortical bone but not within the mineralized matrix[12]. Furthermore, PLN-deficient mice had fewer TEs within osteocyte canaliculi[12], lower

canalicular drag forces, and decreased responses to exogenous loading[13]. Together, these studies identified PLN as a component of the tethering complex in osteocytes necessary for anabolic responses to mechanical loading. While this finding helped explain how force is transmitted to the osteocyte cell membrane, the PLN-containing tethers must attach to the cell surface to induce biochemical responses.

Intracellular calcium (Ca^{2+}) influx is a potent signal in response to force[14]. Ca^{2+} influx is regulated by voltage sensitive Ca^{2+} channels (VSCCs), and *in vitro* and *in vivo* studies have shown that VSCCs are necessary for anabolic responses to skeletal loading[15,16]. As PLN deficiency impairs mechanically-induced Ca^{2+} signaling in bone[17], we hypothesized that PLN tethers bind VSCC ectodomains, forming what we call a matrix-channel tethering complex (M-CTC), and that this interaction facilitates intracellular Ca^{2+} influx in response to mechanical force.

VSCCs are integral membrane proteins composed of the pore-forming α_1 subunit, which enables calcium (Ca^{2+}) entry, and auxiliary subunits including $\alpha_2\delta$, β, and γ[18] **(Fig. 1)**. While the pore-forming (α_1) subunit enables Ca^{2+} entry across the membrane, auxiliary subunits influence gating kinetics of the channel pore. In particular, the $\alpha_2\delta_1$ subunit is anchored in the plasma membrane, with the majority of the protein positioned extracellularly, an optimal location to interact with extracellular molecules, such as PLN-containing tethering elements. Interestingly, the $\alpha_2\delta_1$ subunit is the binding site of the antiepileptic and neuropathic pain drug gabapentin (GBP)[19,20] (**Fig. 1**). Chronic GBP use is associated with increased fracture risk in humans[21] and impaired bone formation in both human and animal studies[22,23]. However, the mechanism(s) mediating GBP-associated adverse skeletal effects are unclear. Thus, in addition to establishing if PLN directly binds the $\alpha_2\delta_1$ subunit of VSCCs, we sought to determine if GBP interferes with binding of the PLN/$\alpha_2\delta_1$ complex.

$\alpha_2\delta_1$ and PLN co-localize in murine osteocyte-like cells. We conducted double immunostaining to test whether PLN co-localizes with the pore-forming $Ca_v3.2$ (α_{1H}) VSCC subunit, with wheat germ agglutinin (WGA), and/or $\alpha_2\delta_1$ in MLO-Y4 osteocytic cells. As we previously reported, $Ca_v3.2$ (α_{1H}) is the primary α_1 VSCC subunit in osteocytes[24]. In MLO-Y4 cells, $Ca_v3.2$ (α_{1H}) is expressed within the cell, but also along the cell periphery (**Suppl. Fig. S1a, d**). As WGA binds N-acetyl glucosamine sugars, which are present on the extracellular α_2 portion of $\alpha_2\delta_1$, we performed double staining with $Ca_v3.2$ and WGA-FITC (**Suppl. Fig. S1a, b**). Areas of overlap (yellow) validated our previous findings that $Ca_v3.2$ associates with $\alpha_2\delta_1$ in osteocytes (**Suppl. Fig. S1c**). To determine if PLN associates with $Ca_v3.2$ (α_{1H}) channels, double staining with $Ca_v3.2$ (α_{1H}) and PLN was performed (**Suppl. Fig. S1d-f**). Several areas of overlapping signal demonstrated that PLN associates with $Ca_v3.2$ (α_{1H}) (**Suppl. Fig. S1f**).

Consistent with these findings, PLN and WGA staining overlapped in areas along the cell membrane (**Fig. 2a-c**). Immunostaining of MLO-Y4 cells using antibodies specific to $\alpha_2\delta_1$ and PLN, demonstrated that both $\alpha_2\delta_1$ (**Fig. 2d**) and PLN (**Fig. 2e**) are produced in osteocytic cells. Merged images showed strong overlapping fluorescent signal of these two proteins (**Fig. 2f**, yellow areas). Importantly, the signal was most prominent along osteocytic processes, demonstrating co-localization of PLN and $\alpha_2\delta_1$ in the area of greatest mechanosensitivity (**Fig. 2d-f**). All cell culture immunostaining assays showed no signal when probed with normal IgG in place of the primary antibodies or when using N, N', N''- triacetylchitotriose as a negative control for WGA-FITC staining. Consistent with the immunostaining results, co-immunoprecipitation assays using MLO-Y4 lysates, showed that $\alpha_2\delta_1$ and PLN interact forming a complex *in vitro* (**Fig. 2g**). Overall, these data suggest that this matrix (PLN)-channel ($\alpha_2\delta_1$) tethering complex is a critical component for mechanosensory responses in osteocytes.

$\alpha_2\delta_1$ and PLN bind with high affinity, which is mediated by PLN Dm III-2. To quantify the molecular interactions between PLN and $\alpha_2\delta_1$ we first tested the binding affinity of full-length PLN protein (native form/undigested and enzymatically digested) and the α_2 portion of $\alpha_2\delta_1$, followed by quantifying the binding affinity of individual PLN domains/subdomains (Dm I, III-2, IV-1, IV-2, IV-3, and V) with α_2. Using LSPR-based experiments (**Suppl. Fig. S2, S3**), we obtained the dissociation constant (the constant describing the drug/receptor interactions at equilibrium) between α_2-bound sensors and PLN. With a dissociation constant (K_D) of 6.6 x 10^{-11} M, full-length PLN (undigested) bound with high affinity to the α_2 portion of $\alpha_2\delta_1$ (**Table 1**). Removal of heparan sulfate and chondroitin sulfate groups from PLN (digested) resulted in a K_D of 2.6 x 10^{-7} M.

When examining the individual domains/subdomains of PLN, Dm III-2 had the greatest affinity to the α_2 polypeptide, displaying a K_D of 8.0 x 10^{-11} M. We also tested binding of α_2 to Dm III-2 followed by a cysteine-rich sequence. We found that the K_D value for this domain was 7.7 x 10^{-6}, suggesting that binding of PLN to $\alpha_2\delta_1$ via Dm III-2 is less likely to be mediated through cysteine rich regions. The K_D values of other PLN domains were, Dm I: 7.7 x10^{-6}, Dm IV-1: 1.4 x 10^{-7}, Dm IV-2: 4.3 x 10^{-4}, Dm IV-3: 1.6 x 10^{-3}, and Dm V: 5.1 x 10^{-3}. These values each demonstrated moderate to weak binding to α_2 (**Table 1**). The raw data used to obtain the final dissociation constant values are provided as supplementary information (**Suppl. Fig. S4**, **Suppl. Table S1**).

To evaluate binding of PLN and $\alpha_2\delta_1$ *in silico*, computational 3D protein-protein docking models between the von Willebrand Factor A (vWFA) domain of $\alpha_2\delta_1$ (4FX5) and PLN domain III-2 (4YEP) were generated. The quality report for structure accuracy confirmed that the models used for receptor (4FX5, 95.7 %) and ligand (4YEP, 100%) had high sequence identities with the input structures, where a sequence ID > 30% is considered reliable. Quality criteria of input protein structures were analyzed by ProQ (v1) (ref. 25), a neural network-based method that predicts the quality of a protein model,

as measured by LGscore or MaxSub[26]. Suitable scores for these parameters are classified as correct (LGscore >1.5; MaxSub > 0.1), good (LGscore ≥3 to <5; MaxSub ≥0.5 to <8) or very good (LGscore ≥ 5; MaxSub ≥ 0.8). Input models for receptor 4FX5 (LGscore = 5.77; MaxSub =0.428) and ligand 4YEP (LGscore = 5.811; MaxSub =0.234) were within the appropriate quality ranges for docking modeling. In the HDOCK server, putative binding modes are ranked according to their binding energy scores[27,28]. The first of the top ten prediction models for 4FX5 and 4YEP scored a docking energy of -272.35, indicating strong protein-protein interactions. Cartoon and surface 3D representations of the highest ranked surface binding prediction model are shown in **Figure 3**.

Gabapentin interferes with PLN:$\alpha_2\delta_1$ binding. Since PLN Dm III-2 showed the highest affinity for α_2, we then used LSPR assays to determine if binding of PLN Dm III-2 or full-length PLN with $\alpha_2\delta_1$ is disrupted by GBP. This was achieved with a series of assays adding either PLN or GBP to the α_2 peptide bound to the nanoplasmonic sensor. With α_2 bound to the nanoplasmonic sensor, we first added full-length PLN, which generated a +14.4 nm shift ($\Delta\lambda$). Subsequent addition of GBP resulted in a -4.1 nm shift, suggesting dissociation of PLN from α_2 in the presence of GBP (**Table 2. Exp. 1**).

Next, instead of first adding PLN to the nanoprism-bound α_2 polypeptide, GBP was added which resulted in a +5.8 nm shift. Binding of GBP, then was followed by addition of full-length PLN which generated a shift of only +0.1 nm, indicating an inability of PLN to bind α_2 in the presence of GBP (**Table 2. Exp. 2**).

Using a third approach, full-length PLN was pre-incubated with GBP, and this combination then was added to the α_2-bound nanoprism. Addition of the PLN/GBP mixture resulted in a +2.7 nm $\Delta\lambda$ shift. As the +2.7 nm shift was similar to the +5.8 nm shift observed with GBP binding α_2 than the +14.4 nm shift found when PLN bound alone, this indicated that in the presence of both GBP and PLN, with equal opportunity to bind, GBP but not PLN bound to the α_2 polypeptide (**Table 2, Exp. 3**).

A similar series of experiments were conducted to quantify the interactions between PLN Dm III-2, α_2, and GBP. Here, α_2 bound with high affinity to Dm III-2 (+12.7 nm shift), and the addition of GBP interfered with this association (-4.3 nm shift) (**Table 2, Exp. 4**). When GBP was bound to α_2 prior to addition of PLN Dm III-2, the presence of GBP restricted binding of Dm III-2 (+0.4 nm shift) to α_2 (**Table 2, Exp. 5**), and incubation of α_2 with a mixture of Dm III-2 and GBP resulted in a shift in the wavelength of +4.9 nm, indicating that GBP bound to α_2, but not PLN Dm III-2 (**Table 2, Exp. 6**).

Gabapentin impairs bone mechanosensation *in vivo*. To determine the effects of GBP on skeletal mechanosensitivity we examined changes in anabolic bone responses to mechanical loading in mice treated with GBP or saline (vehicle, VEH). At the time of experiment mice in the VEH and GBP groups had body weights of 29.3 ± 0.41and 29.9 ± 0.43 g, respectively (mean ± SEM). The body weight was not different between groups (p=0.41) and remained stable over the 4 weeks of treatment. In VEH treated mice, as expected, dynamic histomorphometry analyses of loaded ulnas revealed a significant increase in periosteal mineralizing surface (MS/BS) (+17.1 %, p=0.005), bone formation rate (BFR/BS) (+40.4%, p=0.004) and mineral apposition rate (+23.5%, p=0.038) compared to non-loaded controls (**Fig. 4a-b, Table 3)**. In contrast, GBP treatment resulted in blunted bone mechanosensitivity and impaired bone formation. While mice treated with GBP had increased MAR (+17.9% vs non-loaded, p=0.012) there was no change in MS/BS (p=0.67) or BFR/BS (p=0.38) following mechanical loading (**Fig. 4a-b, Table 3)**. The final number of animals included in the analysis was n=9 for the VEH-treated mice and n=7 for the GBP treated mice. One animal from the GBP group was euthanized before completion of the experiment (broken ulna during initial loading) and another mouse from the same group was removed due poor histological quality of control (non-loaded) sections, and thus inability to conduct proper paired comparisons.

Discussion

Mechanotransduction requires physical coupling of mechanosensory components and the ability of those components to transduce mechanical signals into biochemical responses[29]. Numerous studies have identified molecules that contribute to mechanical signaling within bone such as sclerostin[30,31], connexins[32-34], and focal adhesions[35-39]. However, the mechanism by which force is directly transmitted from the bone matrix to the osteocyte cell membrane remains unclear. Likewise, while the presence of transverse TEs in osteocytes has been established[11,13,24,40], the cell membrane molecules to which PLN-containing tethers bind is unknown.

Our hypothesis that PLN binds to the $\alpha_2\delta_1$ subunit of VSCCs was formed through several observations. First, various studies showed that VSCCs regulate skeletal mechanosensitivity[16,41,42]. Second, spatial positioning of $\alpha_2\delta_1$ is optimal for interaction with PLN, in that $\alpha_2\delta_1$ has a large extracellular region (α_2) capable of interacting with ligands. And third, the ability of $\alpha_2\delta_1$ to regulate gating kinetics of the α_1 pore of VSCCs[43] made $\alpha_2\delta_1$ a strong candidate receptor for PLN binding. Our data showed that PLN matrix tethers bind $\alpha_2\delta_1$ with high affinity, connecting the mineralized bone matrix with the osteocyte cell membrane (**Fig. 5a**).

We previously demonstrated that $\alpha_2\delta_1$ modulates mechanically-regulated ATP release in osteocytes via its association with $Ca_v3.2$ (α_{1H}), the predominant α_1 pore-forming subunit within these cells[24,44]. The extracellular portion (α_2) of the $\alpha_2\delta_1$ subunit is known to be glycosylated with N-acetyl glucosamine sugars. These glycosylation sites are essential for surface expression of $\alpha_2\delta_1$ and have high affinity to WGA[45]. In this work we confirmed expression of α_{1H} in MLO-Y4 cells and found that PLN staining independently overlapped with α_{1H} and WGA fluorescent signals at the cell surface of osteocytic cells, suggesting close physical proximity of PLN and the α_{1H} pore and the sugars attached to $\alpha_2\delta_1$. In addition, $\alpha_2\delta_1$ and PLN co-localize in osteocytic cells along

the dendritic processes of osteocytes, the area most sensitive to mechanical force[46]. Furthermore, by quantifying the molecular interactions between the extracellular portion of $\alpha_2\delta_1$ and different PLN domains/subdomains, we demonstrated that $\alpha_2\delta_1$ and PLN binding is facilitated within the cysteine-free region of PLN Dm III-2, with K_D values in the low nanomolar range compared to other PLN subdomains, showing K_D values in the milli- and micromolar ranges. As a reference, binding of biotin and avidin is among the strongest non-covalent affinities known[47] with a dissociation constant of about 1.3×10^{-15}. This aligns with literature reports in which Dm III mediates the binding of other molecules with PLN, including the fibroblast growth factor (FGF)-7 (N-terminal half of Dm III)[48], platelet-derived growth factor (PDGF) (Dm III-2)[49], and FGF18 (Dm III, cysteine-free region)[50]. Further, previous work showed that PLN binds to another matrix molecule called von Willebrand Factor A-domain-Related Protein (WARP)[51]. Notably, the interaction between WARP and PLN is mediated through Dm III-2 of PLN and the von Willebrand Factor A (vWFA) domain of WARP[51]. As the α_2 portion of the $\alpha_2\delta_1$ subunit contains a vWFA domain[52] which enables binding to extracellular matrix molecules[53], these findings provided further reasoning that PLN and $\alpha_2\delta_1$ form a functional complex.

In silico docking models between the vWFA domain of α_2 and PLN Dm III-2 predicted strong interactions between these molecules. Although there are limitations in the interpretation of HDOCK results[27,28], the quality results for structure accuracy indicate that the docking predictions obtained are reliable. Our 3D models, combined with the LSPR data, confirm that Dm III-2 is a binding site for α_2, mediating the interaction of the PLN/$\alpha_2\delta_1$ complex. Together, this M-CTC, composed of PLN and $\alpha_2\delta_1$, is thus spatially, structurally, and biochemically positioned to activate osteocytes in response to mechanical force (**Fig. 5a**).

Whereas several clinical studies link chronic use of GBP with adverse skeletal side effects, including increased fracture risk[22,54], the molecular mechanisms underlying these

effects and whether they occur directly in bone are entirely unknown. We hypothesized that GBP disrupts PLN/$\alpha_2\delta_1$ binding, affecting the function of the M-CTC, which may explain the skeletal side effects of this medication. GBP recognizes an Arg-Arg-Arg (RRR) motif within the α_2 region of the $\alpha_2\delta_1$ subunit[20], located upstream and in close proximity to the vWFA domain **(Fig. 1)**. Interactions occurring in regions flanking the vWFA can restrict the conformation of the domain (i.e., close, low affinity vs open, high affinity ligand binding states)[55]. Thus, binding of GBP to the RRR motif may disrupt vWFA-mediated interactions of $\alpha_2\delta_1$ with other proteins, such as was demonstrated in a recent study where GBP blocked binding of $\alpha_2\delta_1$ and thrombospondins[56]. Here, we demonstrated that GBP interferes with binding of PLN (full-length and Dm III-2) and $\alpha_2\delta_1$ *in vitro*, effectively uncoupling the M-CTC (**Fig. 5b**). We also showed that acute GBP treatment in mice blunts the anabolic bone responses to mechanical loading. Previous studies have shown that both PLN[13] and $\alpha_2\delta_1$ (ref. 24) are necessary for mechanotransduction in skeletal cells. Thus, GBP may impair osteocyte mechanosensation by disrupting the function of the PLN::$\alpha_2\delta_1$ complex and contribute to the deleterious skeletal effects observed with chronic use of these drugs[21-23].

Limitations of this study include the use of only male mice for evaluating the *in vivo* effects of GBP on bone. Ongoing work is focused on understanding the tissue level impact of GBP in female mice. Furthermore, we did not assess binding of PLN Dm II with $\alpha_2\delta_1$. However, as we found that Dm III-2 bound with equivalent affinity to that of full-length PLN, we were confident that the observed binding between the full-size core protein of PLN was mediated through Dm III-2. Additionally, in contrast to that of PLN Dm III and $\alpha_2\delta_1$, there are no previous studies that support a potential interaction between Dm II and $\alpha_2\delta_1$.

Notable strengths of this work included the use of LSPR-based experiments to determine the interactions between PLN and $\alpha_2\delta_1$. In this regard, the nanoplasmonic

sensors provided reproducible limit of detection at the low zeptomolar range, along with quantitative dissociation constant values (K_D) between biomolecules[57,58] with far greater sensitivity than conventional SPR methods. Additionally, while our interest in the M-CTC lie in osteocyte physiology, it is likely that the function of this complex is conserved across numerous tissues. As such, identification of this novel mechanosensory complex may have a dramatic impact on understanding how other tissues regulate mechanosensation, especially as PLN serves mechanotransduction functions in other cell types[59].

In summary, this work identified novel interactions between the large heparan sulfate proteoglycan PLN and an extracellular auxiliary subunit of VSCCs. Formation of this complex revealed how the transverse tethers previously identified as force transducers in osteocytes attach to the cell membrane, but also provided a greatly expanded understanding of how VSCCs are capable of being activated by mechanical force. Most importantly, our data demonstrate how GBP may negatively regulate bone remodeling by interfering with osteocyte mechanosensation. Better understanding of the mechanisms by which GBP regulates skeletal mechanotransduction will guide the treatment of patients using these drugs and may lead to the design of precision agents efficacious at their target tissues, but devoid of detrimental skeletal effects.

Materials and Methods

Cell culture and immunofluorescence. Immunofluorescence experiments were performed using the osteocytic cell line MLO-Y4. Approximately 1,000 MLO-Y4 cells were seeded onto collagen-I coated 8-well chambers (NUNC™, Rochester, NY) and cultured as described previously[60]. When cells were 80-90% confluent, media was removed, cells were washed with Tris-buffered saline (TBS) and fixed with paraformaldehyde (4%, v/v) diluted in TBS for 45 min at room temperature (RT). Cells

were washed with TBS to remove residual fixative and incubated for 1h at RT in donkey serum (5%, v/v) diluted in TBS with Tween 20 (0.1 %, v/v). Cells were incubated with the appropriate primary antibodies (Abs) diluted in blocking buffer for 1h at RT. For co-localization experiments, where association between $Ca_v3.2$ (α_{1H}), $\alpha_2\delta_1$, and PLN were performed in osteocytic cells, the following primary Abs were used: affinity-purified rabbit anti-$Ca_v3.2$ (α_{1H}) polyclonal antibody (1:100) was raised against a synthetic peptide sequence and prepared for our laboratory commercially by ResGen (Invitrogen, Carlsbad, CA, USA), as described[61]. Staining for $\alpha_2\delta_1$ was performed as previously reported[24], affinity purified rabbit anti-$\alpha_2\delta_{1A}$ isoform polyclonal antibody (1:500) produced by Bethyl Laboratories (Montgomery, TX)[62] was used. For PLN staining, cells were incubated with rat monoclonal anti-PLN domain-IV (A7L6) primary antibody (1:40) (Abcam, Boston, MA, USA). Following incubation with the primary Abs, cells were washed with blocking solution and incubated with species-specific Alexa Fluor 488 and 555 conjugated secondary Abs (1:200) (Invitrogen, Carlsbad, CA, USA) and DRAQ5™ nuclear stain (1:1000) (Biostatus, Ltd, Shepshed Leicestershire, UK) diluted in blocking solution. To visualize cell membrane glycoproteins, cells were stained with fluorescein conjugated wheat germ agglutinin (WGA) (Invitrogen, Carlsbad, CA, USA). Samples were washed with TBS, mounted, and stored at 4°C until imaged. Negative controls for cultured cells were performed using non-immune IgGs diluted at concentrations equivalent to primary Abs or without primary Abs. For cells stained with WGA, an N, N', N''- triacetylchitotriose control was used. Samples were imaged with an LSM 510 VIS confocal microscope using a 40X C-apochromat water immersion objective (NA 1.2) (Zeiss, Inc, Thornwood, NY).

Co-immunoprecipitation and western blotting. To determine if $\alpha_2\delta_1$ associates with PLN, co-immunoprecipitation assays were performed. MLO-Y4 cells (~90% confluent)

353 cultured on 100 mm dishes were exposed to 500 µL of radio immunoprecipitation (RIPA)
354 lysis buffer containing a protease inhibitor cocktail added just prior to cell lysis (1:100)
355 (Sigma-Aldrich, USA). Plates were incubated with lysis buffer at 4°C for 1 min. Lysates
356 were scraped from each plate and placed in 1.5 mL tubes. Samples were sonicated and
357 centrifuged (14,000 g) for 10 min at 4°C. Protein concentration was determined using the
358 Pierce BCA protein assay kit (ThermoFisher Scientific, MA, USA). Samples were diluted
359 in RIPA buffer to achieve equal protein concentrations. Pre-cleared lysates were added
360 to 100 µL of magnetic Dynabeads (Invitrogen, Carlsbad, CA, USA) complexed to 5 ug of
361 monoclonal anti-PLN A7L6 antibody (Abcam, Boston, MA, USA) or Rat IgG. Lysates and
362 beads were incubated on a rotator at RT for 45 min. The Dynabead-Ab-Ag complex was
363 washed three times with 1X phosphate-buffered saline (PBS). Beads then were
364 resuspended in PBS and the supernatant was transferred to a new tube. Supernatants
365 were diluted in Laemmli buffer containing β-mercaptoethanol (2%, v/v) and boiled for 10
366 min. Western blotting was performed as described[38]. Equal volumes of each sample (20
367 µL) were electrophoresed in 8-12% Tris-Acetate gels and probed with the anti-$\alpha_2\delta_{1A}$
368 (Bethyl Laboratories) and anti-PLN A7L6 (Abcam, Boston, MA, USA) primary antibodies
369 (1:500). Blots were probed for β-actin Ab (Cell signaling) (1:500) as a loading control.
370
371 ***Recombinant $\alpha_2\delta_1$ polypeptides.*** The α_2 portion of the human $\alpha_2\delta_1$ protein (NCBI
372 reference sequence NP_00713.2) was produced by *GenScript Protein Expression and*
373 *Purification Services* (GenScript Corp, Piscataway, NJ). Briefly, the α_2 target DNA
374 sequence was designed, optimized, and synthesized by sub-cloning into a pcDNA3.4
375 vector and transfection-grade plasmid was maxi-prepared for cell expression. Expi293F
376 cells were grown in serum-free Expi293FTM Expression Medium (ThermoFisher
377 Scientific, MA, USA). Cells were maintained in Erlenmeyer flasks (Corning, NY, USA) at
378 37°C with CO_2 (8% v/v) on an orbital shaker (VWR Scientific). One day before

transfection, cells were seeded at an appropriate density in flasks. On the day of transfection, DNA and transfection reagent were mixed at an optimal ratio and added to the cells. The recombinant plasmid encoding the target protein was transiently transfected into Expi293F cells. Culture supernatants, collected on day 6, were used for protein purification. Conditioned media was centrifuged, filtered, then passed through a HisTrapTM FF crude affinity purification column at an appropriate flowrate. After washing and elution with appropriate buffers, the eluted fractions were pooled, and buffer exchanged to the final formulation buffer. Purified protein was analyzed by western blot to confirm the molecular weight and purity. The concentration was determined by Micro-Bradford assay with BSA as a standard (ThermoFisher Scientific, MA, USA). Purified protein was stored in 1x PBS (pH 7.2), filter sterilized (0.22 µm), and packaged aseptically at a concentration of 37 µg/mL.

Full-length perlecan and perlecan domains I, III, IV-1, IV-2, IV-3, and V. Full-length PLN was isolated and purified from HT-29 human colorectal cancer cells (formerly called WiDr) (ATCC, Manassas, VA, USA) as reported[63,64] (**Suppl. Methods**). PLN domains (Dm) I, Dm IV-1, Dm IV-2, and Dm IV-3 (ref. 63, 65, 66) and Dm V (ref. 67), were produced and purified as described previously (**Suppl. Methods**). PLN Dm-III is composed of three cysteine-free, laminin-like globular domains with alternating laminin EGF-like cysteine-rich regions[68]. We designed two Dm-III plasmids using SnapGene, the first encoding the cysteine free, globular region of PLN Dm III-2 (laminin IV-A2) and the second Dm III-2 (IV-A2) followed by a cysteine-rich laminin EGF-like region (Dm III-2 + cysteine). Each contained an EF-1α promoter and BM40 signal sequence for enhanced secretion, as well as a C-terminal FLAG tag and 6x His-tag for purification (VectorBuilder, IL, USA). Plasmids were transfected into HEK293A cells using Lipofectamine 2000 (Life Technologies, CA, USA). Transfected cells were grown from

single-cell clones and selected with G418 (2 mg/mL). Dm III-2 and Dm III-2 + cys production was confirmed via western blot using 6x His-tag Ab (Invitrogen, Carlsbad, CA, USA). Positive clones were expanded, purified, and sequenced for verification. Conditioned media from hyperflasks was collected and concentrated in bulk using the Sartorius Vivaflow Cross-flow System (Sartorius, NY, USA) with Vivaflow 200 10,000 MWCO PES filters (Sartorius, NY, USA). Dm III-2 and Dm III-2 + cys were purified using Ni-NTA resin as described for Dm IV recombinant proteins **(Suppl. Methods)** with one additional wash of 500 mM NaCl after conditioned medium flow through and before the imidazole (20 mM) wash. The purified protein was buffer exchanged and stored at -80°C.

Localized surface plasmon resonance (LSPR) experiments. The LSPR-based assay was used to delineate the region of each protein necessary for the structural integrity of the matrix-channel tethering complex (M-CTC), which enabled quantification of the binding interaction between full-length PLN, recombinant subdomains of PLN, and the α_2 portion of the $\alpha_2\delta_1$ subunit. In brief, noble metal nanoparticles display unique localized SPR properties, which are dependent on the size and shape[69-71], and most importantly, the dielectric constant of their surrounding environment[72,73]. Utilizing the latter dependency, solid-state, LSPR-based sensors have been developed employing simple optical spectroscopy to detect biological constituents by monitoring the LSPR changes ($\Delta\lambda$) induced by their presence[58,74]. A schematic representation of LSPR experiments is summarized in **Supplementary Figure S2**. ***Synthesis of gold triangular nanoprisms (Au TNPs).*** Au TNPs were chemically synthesized according to published procedures[75-77]. Briefly, 10.4 mg (0.05 mM) of $Et_3Pau(I)Cl$ were dissolved in N_2 purged acetonitrile (20 mL) and stirred at RT for 5-10 min. Then, 19 µL (0.273 mM) of triethanolamine (TEA) was added to the solution and heated. Upon solution temperature reaching 38 °C, 300

μL of polymethylhydrosiloxane (PMHS) was added, and the reaction slowly stirred. During the reaction, the solution color changed gradually from colorless to dark navy-blue, indicating the formation of Au TNPs. Once a dark navy-blue color was achieved, the LSPR dipole peak position (λ_{LSPR}) was monitored through UV-visible spectroscopy until the solution was λ_{LSPR} = ~800 nm, indicating the formation of ~42 nm edge length Au TNPs (***SI appendix,* Fig. S3**). The Au TNP solution was centrifuged at 7,000 rpm for 10 s, transferred to 3-mercaptopropyltrimethoxysilane (MPTMS)-functionalized glass coverslips (***SI appendix,* Suppl. methods**) and incubated for 1 h. TNP bound coverslips were rinsed with acetonitrile, dried with N_2 gas, and stored under N_2 at 4°C. Au TNP-bound coverslips were used within 3 days of the attachment**. *α_2-functionalized Au TNPs*.** Au TNP-bound glass coverslips underwent a tape-cleaning procedure to remove non-prismatic structures. Briefly, 3M adhesive tape was placed onto the Au TNP-bound glass coverslip, pressed gently with the thumb, and then the tape was removed at a 90^0 angle. Cleaned Au TNP-bound coverslips were cut into 6.25 mm x 25 mm pieces using a diamond cutter to produce the sensors (**Suppl. Fig. S2a**). Each sensor was incubated in 6.0 mL of a 1.0 mM:1.0 μM ratio of 11-mercaptoundecanoic acid (MUDA): 1-nonanethiol (NT) solution overnight (**Suppl. Fig. S2b**). The following day, the sensors were rinsed with ethanol to remove loosely bound thiols. This thiol treatment created a self-assembled monolayer (SAM) onto Au TNP surface. Next, SAM-modified Au TNPS were incubated in an EDC/NHS (0.2 M) solution for 2 h to activate the acid group of MUDA, rinsed with ethanol and PBS, and incubated overnight in a PBS buffer solution (pH 7.2) containing the α_2 portion of $\alpha_2\delta_1$ (10 ng/mL) (**Suppl. Fig. S2c**). To determine the dissociation constant (K_D) values for interactions between α_2 and PLN, each α_2-functionalized sensor was rinsed with PBS and incubated in a solution containing different concentrations ($1x10^{-16}$ to $1x10^{-8}$ M) of full-length PLN (digested with heparanase and chondroitinase, or undigested) or each of PLN domains/subdomains

Dm I, III-2 (cys free), III-2 (cys), IV-1, -2 and -3 or V (**Suppl. Fig. S2d**). At the end of the experiments, the sensors were removed for data collection. Once we established the regions of PLN that mediate binding within the M-CTC, assays were repeated with the addition of GBP (see *drug binding experiments*). ***Protein binding curves and spectroscopy characterization.*** Before and after each incubation step, an extinction spectrum of the sensor was collected through UV-visible spectroscopy, and the shift in the LSPR dipole peak position ($\Delta\lambda_{LSPR}$) was obtained (**Suppl. Fig. S2e**, **S3**). All absorption and extinction spectra were collected utilizing a Varian Cary 50 Scan UV-visible spectrometer in the range of 300-1,100 nm, using 1 cm quartz cuvettes. All spectra were collected in ethanol or PBS (pH 7.2) to keep the bulk refractive index constant. The "background" was a coverslip immersed in ethanol/PBS. The reference (blank) was a sensor incubated in ethanol/PBS (no analyte present). Scanning electron microscopy (SEM) images of Au TNPs were characterized using a JEOL 7800F SEM. ***Data Processing.*** For all UV-vis extinction spectra, λ_{LSPR} was determined through curve fitting using OriginLab software. The $\Delta\lambda_{LSPR}$ was calculated by taking the difference between the λ_{LSPR} before and after each fabrication step. $\Delta\lambda_{LSPR}$ values were reported as the Mean ± standard deviation (SD) of six individual measurements at each concentration used. Using the statistics software GraphPad Prism, protein binding curves were developed by plotting $\Delta\lambda_{LSPR}$ versus PLN [or PLN subdomains] concentration in mol/L (M) (**Suppl. Fig. S2f**). Binding curves were fitted to a specific binding Hill slope (**Suppl. methods**) to determine the K_D values between α_2 and PLN domains/subdomains.

Drug binding experiments. LSPR-based experiments were also used to determine the interactions among α_2, PLN, and GBP. Three different approaches were performed. First, to determine if GBP was capable of displacing PLN from α_2 following binding of PLN to

α_2, the α_2-functionalized sensors were incubated overnight with full-length PLN (10 nM) or PLN Dm III-2 (100 nM), followed by overnight incubation with GBP (0.33 mg/mL). Second, to determine if PLN could displace GBP from α_2, the α_2-functionalized sensors were incubated overnight with GBP (0.33 mg/mL), followed by overnight incubation with full-length PLN (10 nM) or PLN Dm III-2 (100 nM). Lastly, to determine if PLN or GBP had greater affinity for α_2 when provided equal opportunity to bind, the α_2-functionalized sensors were incubated overnight in a mixture of full-length PLN (10 nM) or PLN Dm III-2 (100 nM) and GBP (0.33 mg/mL). At the end of the experiments, sensors were removed for data collection and processing as described above.

3D docking models. *In silico* protein-protein, functional interactions and 3D docking models between the vWFA domain of $\alpha_2\delta_1$ and domain III-2 of PLN were simulated with the free web HDOCK[27,28] server (http://hdock.phys.hust.edu.cn/). To develop high confidence homology models of protein structures, multiple sequence alignment was conducted using Clustal Omega (1.2.4) (ref. 78) (https://www.ebi.ac.uk/Tools/msa/clustalo/). For PLN, the sequences of the three Laminin-IV A subdomains in PLN Dm III [P98160 residues 538-730 (Dm III-1); 941-1125 (Dm III-2), and 1344-1529 (Dm III-3)] were aligned first. Then, the sequence of PLN Dm III-2 [P98160, residues 941-1125] was selected to be aligned against the sequences of the Laminin IV type A1 (P24043; residues 531-723) and Laminin IV type A2 (P24043; residues 1176-1379) domains of Laminin alpha-2. For the vWFA domain, the sequences of the vWFA domains of human thrombospondin 1 (P07996; residues 316-373), thrombospondin 2 (P35442, residues 318-375) and $\alpha_2\delta_1$ (residues 253–430 of CACNA2D1 [P54289]) were used for ClustalO alignment. The amino acid sequences for the vWFA domain of the α_2 peptide (residues 253–430 of CACNA2D1 [P54289]) and PLN Dm III-2 (residues 941-1125 of HSPG2 [P98160]) were input into the protein fold

509 recognition server Phyre2 (ref. 79) to obtain structural 3D models using known protein
510 templates. The structures with the higher model confidence (the probability that the
511 match between the input sequence and the template is a true homology) and I.D. value
512 (the percentage identity between the input sequence and the template) were chosen for
513 docking. The protein template information and 3D structures were retrieved from the
514 RCSB protein data bank (https://www.rcsb.org/). For the vWFA domain of $\alpha_2\delta_1$, the
515 structure of the von Willebrand factor type A from Catenulispora acidiphila (4FX5)
516 (https://www.rcsb.org/structure/4FX5) was selected. For PLN Dm III-2, the structure of
517 the L4b domain of human Laminin alpha-2 (4YEP) (ref. 80)
518 (https://www.rcsb.org/structure/4YEP) was used as the best match. In the HDOCK
519 server, PDB files for 4FX5 (vWFA) and 4YEP (PLN Dm III-2) were used to populate the
520 information for receptor and ligand, respectively. The output with the highest docking
521 energy score from the top 10 predictions was selected for visualization.
522
523 ***Animal experiments and in vivo ulnar loading.*** Male C57BL/6J mice were purchased
524 from the Jackson Laboratory (JAX, Bar Harbor, Maine) and group-housed (2–4
525 mice/cage) on TEK-fresh bedding in ventilated cage systems at the Indiana University
526 School of Medicine animal facilities. Food and water were provided *ad libitum* and mice
527 were maintained under 12-h light/dark cycles and standard conditions of temperature
528 and humidity. At 16 weeks of age, mice were randomly assigned into 2 groups to receive
529 daily intraperitoneal injections of saline (vehicle, VEH) or gabapentin (GBP, 300mg/kg
530 BW; 50mg/mL stock diluted in saline) (Acros Organics AC458020050, ThermoFisher
531 Scientific, MA, USA) for 4 weeks (n=9 mice/treatment). Sample size calculations were
532 based on published data to detect histomorphometrically-measured changes in bone
533 formation induced by loading of 100 $\mu m^3/\mu m^2/yr$, and a true difference between loaded
534 and non-loaded bones as small as 40 $\mu m^3/\mu m^2/yr$ (α=0.05 level; power (1–β) = 80%).

GBP and VEH treated mice were subjected to axial ulnar compression to induce anabolic skeletal responses as previously described[30]. Briefly, mice were anesthetized under gas isoflurane and the right ulna was loaded using a sinusoidal (haversine) waveform (-2200 με, 2 Hz, 180 cycles). Mice received one loading bout every other day over a 10-day period, loading order of mice was randomized each time. Left ulnas were used as non-loaded, contralateral controls. To monitor load-induced bone formation, the fluorochromes calcein (10 mg/kg, Sigma-Aldrich, USA) and alizarin (20 mg/kg, Sigma-Aldrich, USA) were injected intraperitoneally one day before the final loading bout and 11 days later, respectively. Mice were euthanized at 20 weeks of age by CO_2 asphyxiation, followed by cervical dislocation. Ulnas were harvested and processed for dynamic histomorphometry as published[30]. All experiments conducted were approved by the Indiana University Institutional Animal Care and Use Committee.

Dynamic histomorphometry. Preparation and histological sectioning of ulnas was conducted by the Histology and Histomorphometry Core within the Indiana Center for Musculoskeletal Health at Indiana University. To detect bone formation changes in double-labeled histological sections, the following parameters were assessed as previously described[30]: periosteal mineralizing surface (MS/BS, %), mineral apposition rate (MAR, μm/day), and bone formation rate (BFR/BS, $\mu m^3/\mu m^2$/day). All measurements were collected such that investigators were blinded to treatment. Statistical analyses were conducted using the GraphPad Prism software version 9.3.1(471) (La Jolla, CA). Paired Student's t tests compared control, contralateral ulnas to loaded ulnas. Results are reported as mean ± standard error of the mean (SEM). Significance level was defined as $p \leq 0.05$.

Data availability: All data generated or analyzed during this study are included in this published article and its supplementary information files.

Acknowledgements: This study was supported by 1R01AR074473-01 and UL1 TR001108 to WRT, Indiana University Research Support Funds Grant to RS and WRT, 1F32AR074893-01 to CSW, and Faculty Research Development funds through Marian University to JMH and WRT.

Conflict of Interest: KEW receives royalties for licensing FGF23 to Kyowa Hakko Kirin Co., Ltd; had previous funding from Akebia, and current funding from Calico Labs. KEW also owns equity interest in FGF Therapeutics. The other authors have nothing to declare.

Author Contributions: PCRF, XY, ANM, TVT, AB, WRT collection/assembly of data. PCRF, XY, ANM, TVT, AB, CSW, KR, GB, DW, AGR, KR, MLN, KEW, KJL, US, JMH, RS MCFC, WRT data analysis/interpretation. MLN, KEW, KJL, US, JMH, RS, MCFC, WRT concept/design. PCRF, MCFC, WRT manuscript writing. All authors have seen and approved the submitted manuscript.

Supplementary Information: Supplementary information accompanies the manuscript on the Bone Research website http://www.nature.com/boneres

References

1 Bonewald, L. F. The amazing osteocyte. *Journal of Bone and Mineral Research* **26**, 229-238, doi:10.1002/jbmr.320 (2011).

2 Wang, L. J. C. o. r. Solute transport in the bone lacunar-canalicular system (LCS). **16**, 32-41 (2018).

3 Rubin, C. & Lanyon, L. Regulation of bone formation by applied dynamic loads. *J Bone Joint Surg Am* **66**, 397-402 (1984).

4 Fritton, S. P., McLeod, K. J. & Rubin, C. T. Quantifying the strain history of bone: spatial uniformity and self-similarity of low-magnitude strains. *J Biomech* **33**, 317-325 (2000).

5 Klein-Nulend, J., Semeins, C. M., Veldhuijzen, J. P. & Burger, E. H. Effect of mechanical stimulation on the production of soluble bone factors in cultured fetal mouse calvariae. *Cell Tissue Res* **271**, 513-517 (1993).

6 You, J. *et al.* Substrate deformation levels associated with routine physical activity are less stimulatory to bone cells relative to loading-induced oscillatory fluid flow. *Journal of Biomechanical Engineering-Transactions of the Asme* **122**, 387-393 (2000).

7 Smalt, R., Mitchell, F. T., Howard, R. L. & Chambers, T. J. Induction of NO and prostaglandin E_2 in osteoblasts by wall-shear stress but not mechanical strain. *American Journal of Physiology* **273**, E751-E758 (1997).

8 Wang, L. *et al.* In situ measurement of solute transport in the bone lacunar-canalicular system. **102**, 11911-11916 (2005).

9 Burra, S., Nicolella, D. P., Jiang, J. X. J. C. & biology, i. Dark horse in osteocyte biology: Glycocalyx around the dendrites is critical for osteocyte mechanosensing. **4**, 48-50 (2011).

10 Han, Y., Cowin, S. C., Schaffler, M. B. & Weinbaum, S. Mechanotransduction and strain amplification in osteocyte cell processes. *Proceedings of the national academy of sciences* **101**, 16689-16694 (2004).

11 You, L. D., Weinbaum, S., Cowin, S. C. & Schaffler, M. B. Ultrastructure of the osteocyte process and its pericellular matrix. *Anat Rec A Discov Mol Cell Evol Biol* **278**, 505-513, doi:10.1002/ar.a.20050 (2004).

12 Thompson, W. R. *et al.* Perlecan/Hspg2 deficiency alters the pericellular space of the lacunocanalicular system surrounding osteocytic processes in cortical bone. *J Bone Miner Res* **26**, 618-629, doi:10.1002/jbmr.236 (2011).

13 Wang, B. *et al.* Perlecan-containing pericellular matrix regulates solute transport and mechanosensing within the osteocyte lacunar-canalicular system. *J Bone Miner Res* **29**, 878-891, doi:10.1002/jbmr.2105 (2014).

14 Hung, C. T., Allen, F. D., Pollack, S. R. & Brighton, C. T. Intracellular Ca2+ stores and extracellular Ca2+ are required in the real-time Ca2+ response of bone cells experiencing fluid flow. *J Biomech* **29**, 1411-1417 (1996).

15 Li, J., Duncan, R. L., Burr, D. B., Gattone, V. H. & Turner, C. H. Parathyroid hormone enhances mechanically induced bone formation, possibly involving L-type voltage-sensitive calcium channels. *Endocrinology* **144**, 1226-1233, doi:10.1210/en.2002-220821 (2003).

16 Li, J., Duncan, R. L., Burr, D. B. & Turner, C. H. L-type calcium channels mediate mechanically induced bone formation in vivo. *J Bone Miner Res* **17**, 1795-1800, doi:10.1359/jbmr.2002.17.10.1795 (2002).

17 Pei, S. *et al.* Perlecan/Hspg2 deficiency impairs bone's calcium signaling and associated transcriptome in response to mechanical loading. *Bone* **131**, 115078 (2020).

18 Dolphin, A. C. Calcium channel auxiliary alpha2delta and beta subunits: trafficking and one step beyond. *Nat Rev Neurosci* **13**, 542-555, doi:10.1038/nrn3311 (2012).

19 Gee, N. S. *et al.* The novel anticonvulsant drug, gabapentin (Neurontin), binds to the alpha2delta subunit of a calcium channel. *J Biol Chem* **271**, 5768-5776 (1996).

637 20 Wang, M., Offord, J., Oxender, D. L. & Su, T. Z. Structural requirement of the
638 calcium-channel subunit alpha2delta for gabapentin binding. *Biochem J* **342 (Pt**
639 **2)**, 313-320 (1999).
640 21 Jette, N. *et al.* Association of antiepileptic drugs with nontraumatic fractures: a
641 population-based analysis. *Arch Neurol* **68**, 107-112,
642 doi:10.1001/archneurol.2010.341 (2011).
643 22 Ensrud, K. E. *et al.* Antiepileptic drug use and rates of hip bone loss in older men:
644 a prospective study. *Neurology* **71**, 723-730,
645 doi:10.1212/01.wnl.0000324919.86696.a9 (2008).
646 23 Sofu, H. *et al.* Should orthopedic surgeons consider the effects of gabapentin
647 administration on bone healing while treating a long bone fracture: experimental
648 study in a rat model. *SICOT J* **2**, 36, doi:10.1051/sicotj/2016028 (2016).
649 24 Thompson, W. R. *et al.* Association of the α2δ1 subunit with Cav3.2 enhances
650 membrane expression and regulates mechanically induced ATP release in MLO-
651 Y4 osteocytes. *Journal of Bone and Mineral Research* **26**, 2125-2139,
652 doi:10.1002/jbmr.437 (2011).
653 25 Wallner, B. & Elofsson, A. Can correct protein models be identified? *Protein*
654 *science* **12**, 1073-1086 (2003).
655 26 Siew, N., Elofsson, A., Rychlewski, L. & Fischer, D. MaxSub: an automated
656 measure for the assessment of protein structure prediction quality. *Bioinformatics*
657 **16**, 776-785 (2000).
658 27 Yan, Y., Zhang, D., Zhou, P., Li, B. & Huang, S.-Y. HDOCK: a web server for
659 protein–protein and protein–DNA/RNA docking based on a hybrid strategy.
660 *Nucleic acids research* **45**, W365-W373 (2017).
661 28 Yan, Y., Tao, H., He, J. & Huang, S.-Y. The HDOCK server for integrated
662 protein–protein docking. *Nature protocols* **15**, 1829-1852 (2020).

29 Thompson, W. R., Rubin, C. T. & Rubin, J. Mechanical regulation of signaling pathways in bone. *Gene* **503**, 179-193, doi:10.1016/j.gene.2012.04.076 (2012).

30 Robling, A. G. *et al.* Mechanical stimulation of bone in vivo reduces osteocyte expression of Sost/sclerostin. *J Biol Chem* **283**, 5866-5875, doi:M705092200 [pii] 10.1074/jbc.M705092200 (2008).

31 Compton, J. T. & Lee, F. Y. A review of osteocyte function and the emerging importance of sclerostin. *J Bone Joint Surg Am* **96**, 1659-1668, doi:10.2106/JBJS.M.01096 (2014).

32 Loiselle, A. E., Paul, E. M., Lewis, G. S. & Donahue, H. J. Osteoblast and osteocyte-specific loss of Connexin43 results in delayed bone formation and healing during murine fracture healing. *Journal of Orthopaedic Research* **31**, 147-154, doi:10.1002/jor.22178 (2013).

33 Cherian, P. P. *et al.* Mechanical Strain Opens Connexin 43 Hemichannels in Osteocytes: A Novel Mechanism for the Release of Prostaglandin. *Molecular Biology of the Cell* **16**, 3100-3106, doi:10.1091/mbc.E04-10-0912 (2005).

34 Uzer, G. *et al.* Gap Junctional Communication in Osteocytes Is Amplified by Low Intensity Vibrations In Vitro. *PLoS ONE* **9**, e90840, doi:10.1371/journal.pone.0090840 (2014).

35 Cabahug-Zuckerman, P. *et al.* Potential role for a specialized β3 integrin-based structure on osteocyte processes in bone mechanosensation. *Journal of Orthopaedic Research*® **36**, 642-652 (2018).

36 Lee, D. Y. *et al.* Oscillatory Flow-induced Proliferation of Osteoblast-like Cells Is Mediated by alpha(v)beta(3) and beta(1) Integrins through Synergistic Interactions of Focal Adhesion Kinase and Shc with Phosphatidylinositol 3-Kinase and the Akt/mTOR/p70S6K Pathway. *Journal of Biological Chemistry* **285**, 30-42, doi:10.1074/jbc.M109.010512 (2010).

37 Sen, B. *et al.* mTORC2 regulates mechanically induced cytoskeletal reorganization and lineage selection in marrow-derived mesenchymal stem cells. *J Bone Miner Res* **29**, 78-89, doi:10.1002/jbmr.2031 (2014).

38 Thompson, W. R. *et al.* Mechanically activated Fyn utilizes mTORC2 to regulate RhoA and adipogenesis in mesenchymal stem cells. *Stem Cells* **31**, 2528-2537, doi:10.1002/stem.1476 (2013).

39 Thompson, W. R. *et al.* LARG GEF and ARHGAP18 orchestrate RhoA activity to control mesenchymal stem cell lineage. *Bone* **107**, 172-180, doi:10.1016/j.bone.2017.12.001 (2018).

40 Yokoyama, Y., Kameo, Y., Kamioka, H. & Adachi, T. High-resolution image-based simulation reveals membrane strain concentration on osteocyte processes caused by tethering elements. *Biomechanics and modeling in mechanobiology* **20**, 2353-2360, doi:10.1007/s10237-021-01511-y (2021).

41 Brown, G. N., Leong, P. L. & Guo, X. E. T-Type voltage-sensitive calcium channels mediate mechanically-induced intracellular calcium oscillations in osteocytes by regulating endoplasmic reticulum calcium dynamics. *Bone* **88**, 56-63, doi:10.1016/j.bone.2016.04.018 (2016).

42 Genetos, D. C., Geist, D. J., Liu, D., Donahue, H. J. & Duncan, R. L. Fluid Shear-Induced ATP Secretion Mediates Prostaglandin Release in MC3T3-E1 Osteoblasts. *Journal of Bone and Mineral Research* **20**, 41-49, doi:10.1359/jbmr.041009 (2005).

43 Dolphin, A. C. Voltage-gated calcium channels and their auxiliary subunits: physiology and pathophysiology and pharmacology. *J Physiol* **594**, 5369-5390, doi:10.1113/JP272262 (2016).

44 Shao, Y., Alicknavitch, M. & Farach-Carson, M. C. Expression of voltage sensitive calcium channel (VSCC) L-type Cav1.2 (alpha1C) and T-type Cav3.2

(alpha1H) subunits during mouse bone development. *Dev Dyn* **234**, 54-62, doi:10.1002/dvdy.20517 (2005).

45 Tétreault, M.-P. *et al.* Identification of glycosylation sites essential for surface expression of the CaVα2δ1 subunit and modulation of the cardiac CaV1. 2 channel activity. *Journal of Biological Chemistry* **291**, 4826-4843 (2016).

46 Wu, D., Schaffler, M. B., Weinbaum, S. & Spray, D. C. Matrix-dependent adhesion mediates network responses to physiological stimulation of the osteocyte cell process. *Proc Natl Acad Sci U S A* **110**, 12096-12101, doi:10.1073/pnas.1310003110 (2013).

47 Wilchek, M. & Bayer, E. A. Introduction to avidin-biotin technology. *Methods in enzymology* **184**, 5-13, doi:10.1016/0076-6879(90)84256-g (1990).

48 Mongiat, M. *et al.* The protein core of the proteoglycan perlecan binds specifically to fibroblast growth factor-7. *Journal of Biological Chemistry* **275**, 7095-7100 (2000).

49 Göhring, W., Sasaki, T., Heldin, C. H. & Timpl, R. Mapping of the binding of platelet-derived growth factor to distinct domains of the basement membrane proteins BM-40 and perlecan and distinction from the BM-40 collagen-binding epitope. *European journal of biochemistry* **255**, 60-66 (1998).

50 Smith, S. M.-L., West, L. A. & Hassell, J. R. The core protein of growth plate perlecan binds FGF-18 and alters its mitogenic effect on chondrocytes. *Archives of biochemistry and biophysics* **468**, 244-251 (2007).

51 Allen, J. M. *et al.* WARP is a novel multimeric component of the chondrocyte pericellular matrix that interacts with perlecan. *J Biol Chem* **281**, 7341-7349, doi:10.1074/jbc.M513746200 (2006).

52 Dolphin, A. C. The alpha2delta subunits of voltage-gated calcium channels. *Biochim Biophys Acta* **1828**, 1541-1549, doi:10.1016/j.bbamem.2012.11.019 (2013).

53 Garcia, K., Nabhani, T. & Garcia, J. The calcium channel alpha2/delta1 subunit is involved in extracellular signalling. *J Physiol* **586**, 727-738, doi:10.1113/jphysiol.2007.147959 (2008).

54 Ensrud, K. E. *et al.* Antiepileptic drug use increases rates of bone loss in older women: a prospective study. *Neurology* **62**, 2051-2057 (2004).

55 Whittaker, C. A. & Hynes, R. O. Distribution and evolution of von Willebrand/integrin A domains: widely dispersed domains with roles in cell adhesion and elsewhere. *Molecular biology of the cell* **13**, 3369-3387 (2002).

56 Eroglu, C. *et al.* Gabapentin receptor alpha2delta-1 is a neuronal thrombospondin receptor responsible for excitatory CNS synaptogenesis. *Cell* **139**, 380-392, doi:10.1016/j.cell.2009.09.025 (2009).

57 Saha, K., Agasti, S. S., Kim, C., Li, X. & Rotello, V. M. Gold Nanoparticles in Chemical and Biological Sensing. *Chemical Reviews* **112**, 2739-2779, doi:10.1021/cr2001178 (2012).

58 Haes, A. J., Hall, W. P., Chang, L., Klein, W. L. & Van Duyne, R. P. A Localized Surface Plasmon Resonance Biosensor:‚Äâ First Steps toward an Assay for Alzheimer's Disease. *Nano Letters* **4**, 1029-1034, doi:10.1021/nl049670j (2004).

59 Guilak, F., Hayes, A. J. & Melrose, J. Perlecan in pericellular mechanosensory cell-matrix communication, extracellular matrix stabilisation and mechanoregulation of load-bearing connective tissues. *International journal of molecular sciences* **22**, 2716 (2021).

60 Kato, Y., Windle, J. J., Koop, B. A., Mundy, G. R. & Bonewald, L. F. Establishment of an osteocyte-like cell line, MLO-Y4. *Journal of bone and mineral research* **12**, 2014-2023 (1997).

61 Shao, Y., Alicknavitch, M. & Farach-Carson, M. C. Expression of voltage sensitive calcium channel (VSCC) L-type Cav1. 2 (α1C) and T-type Cav3. 2 (α1H) subunits during mouse bone development. *Developmental dynamics: an official publication of the American Association of Anatomists* **234**, 54-62 (2005).

62 García, K., Nabhani, T. & García, J. The calcium channel α2/δ1 subunit is involved in extracellular signalling. *The Journal of physiology* **586**, 727-738 (2008).

63 Grindel, B. *et al.* Matrilysin/matrix metalloproteinase-7 (MMP7) cleavage of perlecan/HSPG2 creates a molecular switch to alter prostate cancer cell behavior. *Matrix Biology* **36**, 64-76 (2014).

64 Tellman, T. V., Cruz, L. A., Grindel, B. J. & Farach-Carson, M. C. Cleavage of the Perlecan-Semaphorin 3A-Plexin A1-Neuropilin-1 (PSPN) Complex by Matrix Metalloproteinase 7/Matrilysin Triggers Prostate Cancer Cell Dyscohesion and Migration. *International journal of molecular sciences* **22**, 3218 (2021).

65 Brasil da Costa, F. H., Lewis, M. S., Truong, A., Carson, D. D. & Farach-Carson, M. C. SULF1 suppresses Wnt3A-driven growth of bone metastatic prostate cancer in perlecan-modified 3D cancer-stroma-macrophage triculture models. *PloS one* **15**, e0230354 (2020).

66 Yang, W., Gomes Jr, R., Alicknavitch, M., Farach-Carson, M. & Carson, D. Perlecan domain I promotes fibroblast growth factor 2 delivery in collagen I fibril scaffolds. *Tissue engineering* **11**, 76-89 (2005).

67 Lee, B. *et al.* Perlecan domain V is neuroprotective and proangiogenic following ischemic stroke in rodents. *J Clin Invest* **121**, 3005-3023, doi:10.1172/JCI46358 (2011).

68 Couchman, J. R., Ljubimov, A. V., Sthanam, M., Horchar, T. & Hassell, J. R. Antibody mapping and tissue localization of globular and cysteine-rich regions of perlecan domain III. *Journal of Histochemistry & Cytochemistry* **43**, 955-963 (1995).

69 Chen, H., Kou, X., Yang, Z., Ni, W. & Wang, J. Shape-and size-dependent refractive index sensitivity of gold nanoparticles. *Langmuir* **24**, 5233-5237 (2008).

70 Sardar, R. & Shumaker-Parry, J. S. Spectroscopic and microscopic investigation of gold nanoparticle formation: ligand and temperature effects on rate and particle size. *Journal of the American Chemical Society* **133**, 8179-8190 (2011).

71 Mulvaney, P. Surface plasmon spectroscopy of nanosized metal particles. *Langmuir* **12**, 788-800 (1996).

72 Joshi, G. K., McClory, P. J., Dolai, S. & Sardar, R. Improved localized surface plasmon resonance biosensing sensitivity based on chemically-synthesized gold nanoprisms as plasmonic transducers. *Journal of Materials Chemistry* **22**, 923-931 (2012).

73 Joshi, G. K. *et al.* Designing Efficient Localized Surface Plasmon Resonance-Based Sensing Platforms: Optimization of Sensor Response by Controlling the Edge Length of Gold Nanoprisms. *The Journal of Physical Chemistry C* **116**, 20990-21000, doi:10.1021/jp302674h (2012).

74 Beeram, S. R. & Zamborini, F. P. Selective Attachment of Antibodies to the Edges of Gold Nanostructures for Enhanced Localized Surface Plasmon Resonance Biosensing. *Journal of the American Chemical Society* **131**, 11689-11691, doi:10.1021/ja904387j (2009).

75 Liyanage, T., Sangha, A. & Sardar, R. Achieving biosensing at attomolar concentrations of cardiac troponin T in human biofluids by developing a label-free nanoplasmonic analytical assay. *Analyst (Cambridge, U. K.)* **142**, 2442-2450, doi:10.1039/c7an00430c (2017).

76 Masterson, A. N. *et al.* A novel liquid biopsy-based approach for highly specific cancer diagnostics: mitigating false responses in assaying patient plasma-derived circulating microRNAs through combined SERS and plasmon-enhanced fluorescence analyses. *Analyst (Cambridge, U. K.)* **145**, 4173-4180, doi:10.1039/d0an00538j (2020).

77 Hati, S. *et al.* Photoswitchable Machine-Engineered Plasmonic Nanosystem with High Optical Response for Ultrasensitive Detection of microRNAs and Proteins Adaptively. *Anal. Chem. (Washington, DC, U. S.)* **93**, 13935-13944, doi:10.1021/acs.analchem.1c02990 (2021).

78 Sievers, F. & Higgins, D. G. Clustal Omega for making accurate alignments of many protein sequences. *Protein Science* **27**, 135-145 (2018).

79 Kelley, L. A., Mezulis, S., Yates, C. M., Wass, M. N. & Sternberg, M. J. The Phyre2 web portal for protein modeling, prediction and analysis. *Nature protocols* **10**, 845-858 (2015).

80 Moran, T., Gat, Y. & Fass, D. Laminin L4 domain structure resembles adhesion modules in ephrin receptor and other transmembrane glycoproteins. *The FEBS journal* **282**, 2746-2757 (2015).

81 Wright, C. S., Robling, A. G., Farach-Carson, M. C. & Thompson, W. R. Skeletal Functions of Voltage Sensitive Calcium Channels. *Current osteoporosis reports* **19**, 206-221 (2021).

Figures Legends

Figure 1. ***Structure of voltage sensitive calcium channels***. The channel complex is composed of the α_1 pore-forming subunit with auxiliary β, γ, and $\alpha_2\delta$ subunits bound to the pore, positioned to alter gating kinetics of the channel. The $\alpha_2\delta$ subunit is anchored in the membrane via the δ portion, with the α_2 region positioned extracellularly. In the extracellular portion (α_2) of the $\alpha_2\delta$ subunit, the von Willebrand Factor A domain (vWFA) sequence and the Arg-Arg-Arg (RRR) motif for Gabapentin binding are indicated. Adapted from Wright *et al.*[81].

Figure 2. ***PLN colocalizes with WGA and $\alpha_2\delta_1$ in osteocyte-like cells*****.** MLO-Y4 cells stained with **(a)** wheat germ agglutinin (WGA)-FITC (green) and **(b)** perlecan (PLN) (red), **(c)** merge PLN and WGA. On the bottom panels, cells were stained for **(d)** $\alpha_2\delta_1$ (red) and **(e)** PLN (green), **(f)** merge PLN and $\alpha_2\delta_1$. White arrows in merged images indicate overlapping fluorescent signal. **(g)** Co-immunoprecipitation assays from MLO-Y4 lysates show that PLN and $\alpha_2\delta_1$ associate. IgG was used as a negative control. Blots were probed for β-actin antibody as a loading control.

Figure 3. ***Docking models of vWFA domain of $\alpha_2\delta_1$ and PLN Dm III-2****. in silico* protein-protein functional interactions and 3D docking models between the von Willebrand Factor A (vWFA) domain of $\alpha_2\delta_1$ and perlecan (PLN) domain (Dm) III-2 were generated with the free web server HDOCK. 4FX5 (brown) is the vWFA domain and 4YEP (yellow) is the L4b domain of human Laminin α_2 (PLN Dm III-2). Top, cartoon ribbon-style 3D representations of receptor and ligand. Bottom, surface style representation of the proteins. Each image is rotated 90° clockwise from the previous one.

Figure 4. ***Gabapentin treatment decreases ulnar mechanosensitivity and load-induced bone formation*** Male C57BL/6J mice were injected daily with saline (vehicle, VEH) (n=9) or Gabapentin (GBP, 300mg/kg BW) (n=7) for 4 weeks while undergoing axial ulnar loading. **(a)** Representative images of control (non-loaded) and loaded ulnas from VEH and GBP treated mice. Changes in **(b)** mineralizing surface (MS/BS), mineral apposition rate (MAR), and bone formation rate (BFR/BS) in response to mechanical loading were assessed in VEH and GBP treated mice. Paired Student's t tests compared control, contralateral ulnas to loaded ulnas. Values are shown as Mean ± SEM; $p \leq 0.01$(**), $p \leq 0.05$(*).

Figure 5. ***Summary of results***. In this work we found that **(a)** the $\alpha_2\delta_1$ subunit of voltage sensitive Ca^{2+} channels binds perlecan (PLN) creating a mechanosensory complex that enables connection between the mineralized matrix and the osteocyte cell membrane. **(b)** We also demonstrated that gabapentin (GBP) interferes with binding of PLN and $\alpha_2\delta_1$ *in vitro*. As the PLN/$\alpha_2\delta_1$ complex is necessary for mechanotransduction, GBP uncoupling of the complex results in impaired osteocyte mechanosensation *in vivo*, which may account for the deleterious skeletal effects observed with chronic use of this drug.

883 **Table 1.** Binding affinity experiments between the α_2 portion of the $\alpha_2\delta_1$ and perlecan

Perlecan Domain / Subdomain	K_D (M)
Undigested Full Length	6.6×10^{-11}
Digested Full Length	2.6×10^{-7}
Domain I	7.7×10^{-6}
Domain III-2	**8.0×10^{-11}**
Domain III-2 (w/cysteine)	7.7×10^{-6}
Domain IV-I	1.4×10^{-7}
Domain IV-2	4.3×10^{-4}
Domain IV-3	1.6×10^{-3}
Domain V	5.1×10^{-3}

884

885 **Table 2.** LSPR-based interactions among α_2-functionalized sensors, PLN and GBP

Exp	Sensors	$\Delta\lambda_{LSPR}$ (nm)	Added first to the sensors	$\Delta\lambda_{LSPR}$ (nm)	Added second to the sensors	$\Delta\lambda_{LSPR}$ (nm)
1	α_2	+39 nm	Full length PLN	+14.4 nm	GBP	-4.1 nm
2	α_2	+39 nm	GBP	+5.8 nm	Full length PLN	+/- 0.1 nm
3	α_2	+39 nm	Full length PLN + GBP	+2.7 nm	-	-
4	**α_2**	**+39 nm**	**PLN Dm III-2**	**+12.7 nm**	**GBP**	**-4.3 nm**
5	**α_2**	**+39 nm**	**GBP**	**+5.4 nm**	**PLN Dm III-2**	**+0.4 nm**
6	**α_2**	**+39 nm**	**PLN Dm III-2 + GBP**	**+4.9 nm**	**-**	**-**

886

887 Exp = Experiment, LSPR = Localized surface plasmon resonance, PLN = Perlecan, GBP

888 = Gabapentin.

889

Table 3. Ulnar dynamic histomorphometry measurements in response to mechanical loading in vehicle and gabapentin treated mice

	VEH[1] treated mice			GBP[1] treated mice		
Bone Parameters[2]	**Non-loaded Ulna (Ctrl)**	**Loaded Ulna**	**p-value[3]**	**Non-loaded Ulna (Ctrl)**	**Loaded Ulna**	**p-value[3]**
MS/BS (%)	72.81 ± 4.7 (9)	85.23 ± 2.2 (9)**	0.005	87.43 ± 5.12 (7)	85.38 ± 2.51 (7)	0.67
MAR (μm/day)	0.976 ± 0.11 (9)	1.21 ± 0.09 (9)*	0.038	1.072 ± 0.08 (7)	1.26 ± 0.08 (7)*	0.012
BFR/BS ($\mu m^3/\mu m^2$/day)	268.5 ± 39.13 (9)	377 ± 34.25 (9)**	0.004	348.9 ± 37.24 (7)	398.1 ± 34 (7)	0.11

[1]Mice were injected with saline (VEH, vehicle) or gabapentin (GBP, 300mg/kg BW) for 4 weeks while undergoing axial ulnar loading. Data are expressed as mean ± SEM (n)

[2]Periosteal mineralizing surface (MS/BS), mineral apposition rate (MAR), bone formation rate (BFR/BS).

[3]Statistical analyses were conducted to detect bone formation changes in response to loading. Paired t-test compared non-loaded controls vs loaded limbs. (**) $p<0.01$; (*) $p<0.05$.

902 **Figure 1**

903

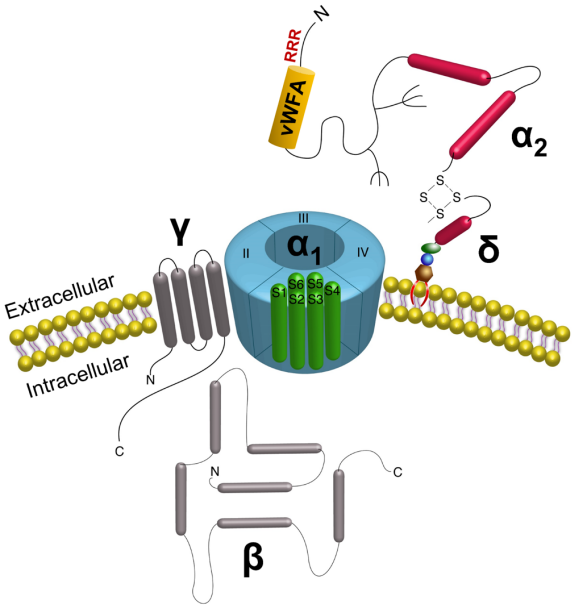

904

905

906 **Figure 2**

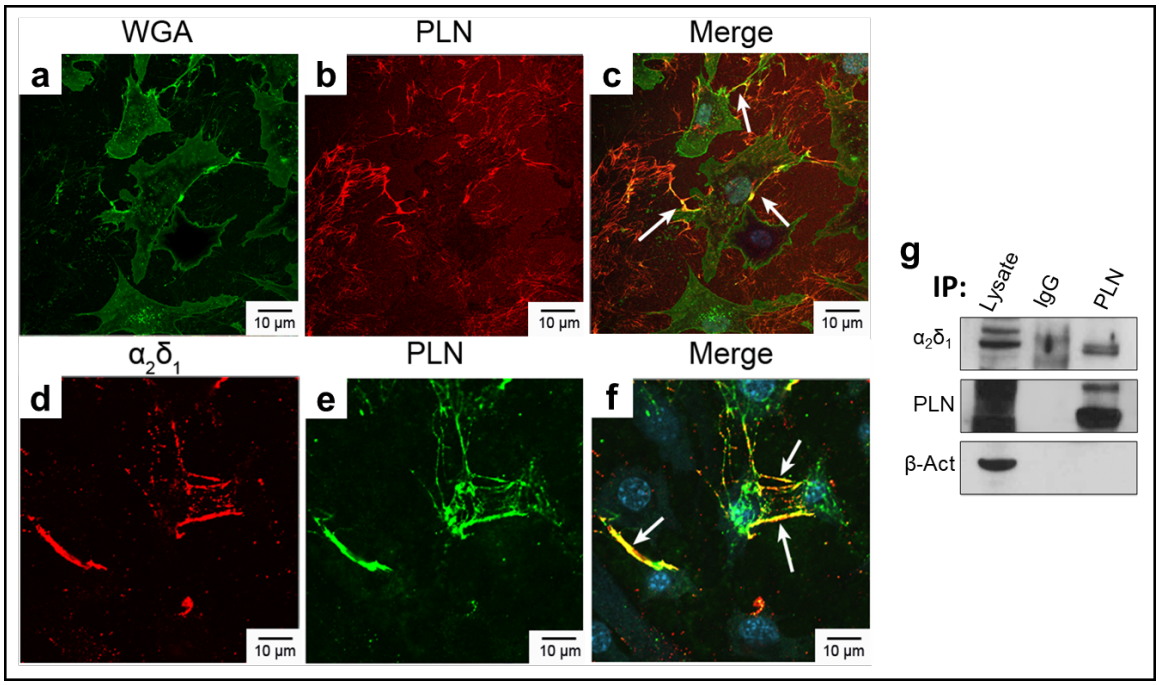

907

908

909 **Figure 3**

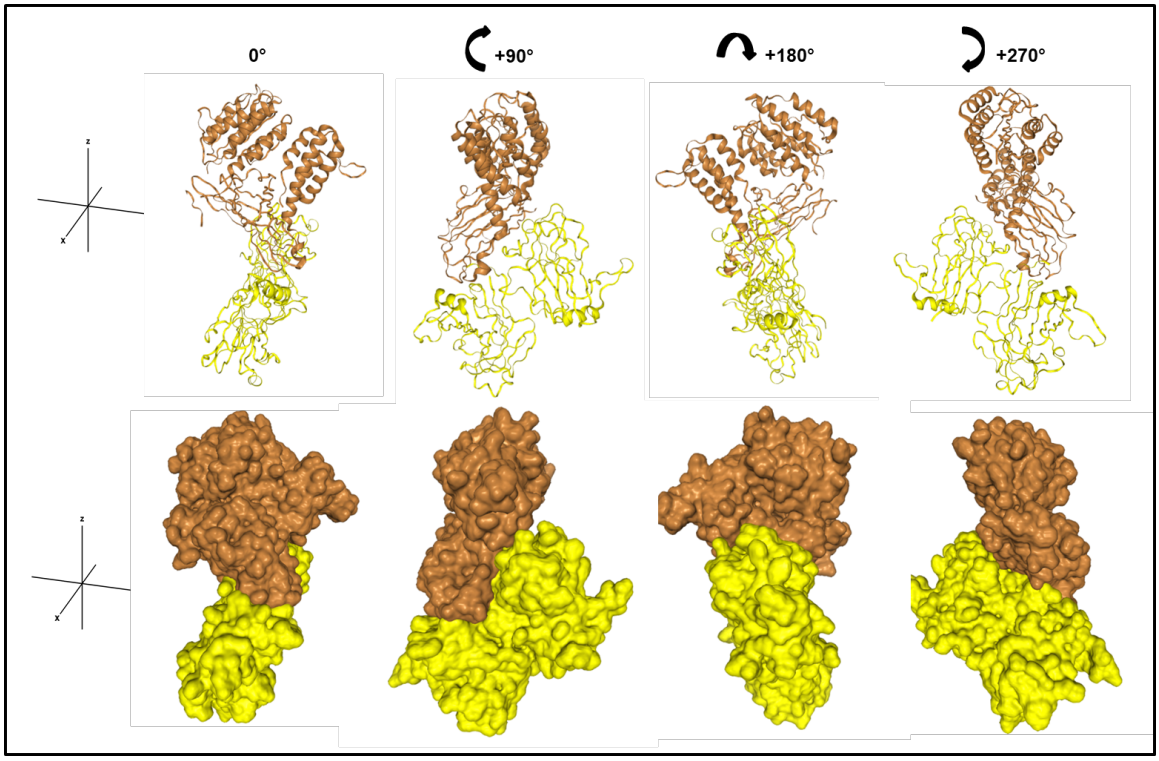

910

911

912 **Figure 4**

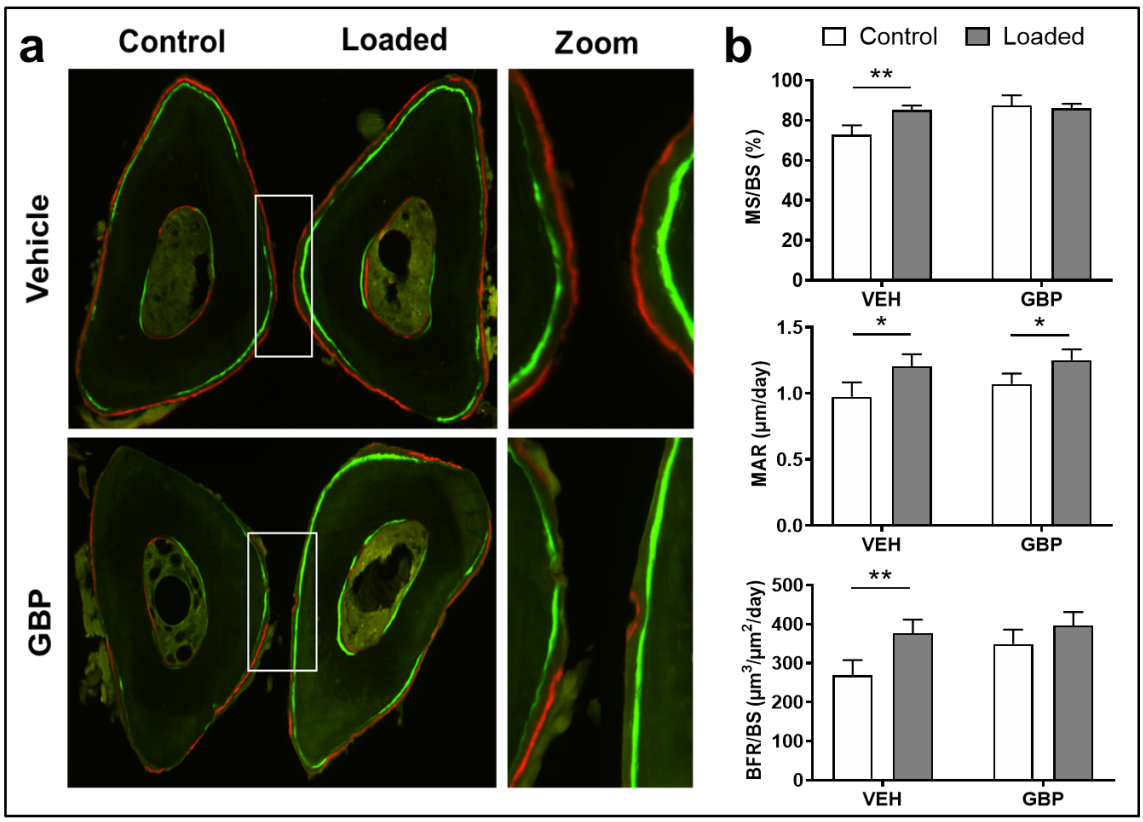

913

914

915 **Figure 5**

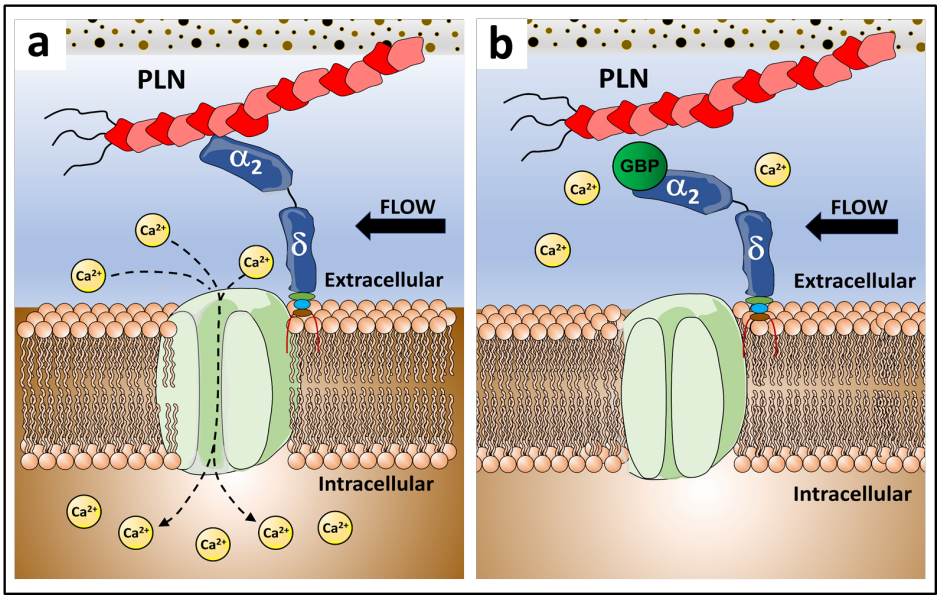

916